

Generation and characterisation of isolated attosecond pulses at 100 kHz repetition rate

Tobias Witting^{1,*}, Mikhail Osolodkov¹, Felix Schell¹, Felipe Morales¹, Serguei Patchkovskii¹, Peter Šušnjar¹, Fabio Cavalcante², Carmen S. Menoni², Claus P. Schulz¹, Federico J. Furch^{1,†} and Marc J. J. Vrakking¹

¹*Max Born Institute for Nonlinear Optics and Short Pulse Spectroscopy, Max-Born-Strasse 2a, 12489 Berlin, Germany*

²*Department of Electrical and Computer Engineering, Colorado State University, Fort Collins, CO 80523, USA*

**email: tobias.witting@mbi-berlin.de*

†email: furch@mbi-berlin.de

The generation of coherent light pulses in the extreme ultraviolet (XUV) spectral region with attosecond pulse durations constitutes the foundation of the field of attosecond science ¹. Twenty years after the first demonstration of isolated attosecond pulses ², they continue to be a unique tool enabling the observation and control of electron dynamics in atoms, molecules and solids ^{3,4}. It has long been identified that an increase in the repetition rate of attosecond light sources is necessary for many applications in atomic and molecular physics ^{5,6}, surface science ⁷, and imaging ⁸. Although high harmonic generation (HHG) at repetition rates exceeding 100 kHz, showing a continuum in the cut-off region of the XUV spectrum was already demonstrated in 2013 ⁹, the number of photons per pulse was insufficient to perform

pulse characterisation via attosecond streaking ¹⁰, let alone to perform a pump-probe experiment. Here we report on the generation and full characterisation of XUV attosecond pulses via HHG driven by near-single-cycle pulses at a repetition rate of 100 kHz. The high number of 10^6 XUV photons per pulse on target enables attosecond electron streaking experiments through which the XUV pulses are determined to consist of a dominant single attosecond pulse. These results open the door for attosecond pump-probe spectroscopy studies at a repetition rate one or two orders of magnitude above current implementations.

Extreme ultraviolet (XUV) light pulses generated via high-order harmonic generation (HHG) ¹¹, consisting of attosecond pulse trains ^{12,13} or isolated attosecond pulses ², have led to the establishment of the field of attosecond science ¹. The HHG process can be described by a very intuitive three-step model ¹⁴, in which the strong electric field of the laser interacting with a gas of atoms first induces tunnel ionisation. The created electron wave packet is accelerated by the electric field of the laser, first away and then back towards its parent ion, and then recombines with the parent ion, releasing the gained kinetic energy in the form of high energy photons at odd multiples of the driving laser frequency. Since the process is repeated every half-cycle of the laser for which the peak intensity is sufficient to ionise the atom, HHG naturally gives rise to a train of attosecond pulses. As the duration of the driving pulse is reduced, the number of pulses in the attosecond pulse train (APT) also decreases. If the driving pulse duration approaches a single oscillation of the optical field, and if it is possible to control the carrier-envelope phase (CEP) of the driving pulses, the XUV emission can be confined to a single half-cycle ^{2,15-17}. Isolated attosecond pulses (IAPs) generated in this manner have been successfully implemented to observe light-induced electron

tunneling in atoms in real time ¹⁸, to follow the valence electron motion in an excited ion ¹⁹, and to control electron localisation in a dissociating molecule with attosecond precision ²⁰, among many other outstanding examples.

In all the aforementioned examples, and in the majority of experimental setups used for attosecond science, the driving pulses for HHG are produced by a Ti:Sapphire chirped pulse amplification (CPA) system followed by non-linear post-compression in a gas-filled hollow-core fibre ²¹, which allows reaching pulse durations near a single optical cycle (2.67 fs at 800 nm) with pulse energies of at least a few hundred μJ . Typical observables in attosecond pump-probe experiments are either the XUV absorption spectrum, or the kinetic energy and/or angular distributions of ions or electrons. While these schemes provide valuable information, many research questions call for more sophisticated experimental approaches. In particular, in experiments with atomic and molecular targets in the gas phase it is highly attractive to implement electron-ion coincidence detection schemes ⁵, which give access to the fully correlated three-dimensional momentum distributions of all charged particles produced during a photoionisation experiment. The technique requires that only one photoionisation event is produced per laser pulse in order to avoid the detection of false coincidences; i.e. ions and electrons that are measured in coincidence, but that originate from different parent atoms/molecules. In practice, this requires working at a maximum event rate of approximately 0.2 times the repetition rate of the light source. It follows that high repetition rate light sources are required for these types of experiments to keep data acquisition times manageable. So far, the implementation of coincidence detection in attosecond experiments has been limited to setups working with Ti:Sapphire CPAs running at $\leq 10\text{kHz}$ ²², where the technique has been suc-

cessfully applied to the study of small molecular systems^{23,24}. However, more complex problems involving the study of low probability ionisation or dissociation channels require higher repetition rates. Furthermore condensed phase experiments such as photoelectron emission microscopy (PEEM)²⁵ and attosecond photoelectron streaking^{7,26} at surfaces would also benefit from high repetition rate attosecond XUV sources. Since a high number of photoelectrons removed from a surface with a single laser shot has detrimental effects on the energy resolution through space-charge effects, it is advantageous to keep the number of photoelectrons generated per shot low. To achieve high signal-to-noise ratio measurements that go beyond proof of principle experiments, increasing the laser repetition rate is the only viable route.

Ti:Sapphire CPAs, delivering CEP-stable, ultrashort pulses with the necessary pulse energies for attosecond pulse generation (typically up to a few mJ) are not scalable beyond 10 kHz. Optical parametric chirped pulse amplifiers (OPCPA)²⁷⁻³² and direct post-compression of high repetition rate ytterbium based CPAs³³⁻³⁵ are viable alternatives capable of generating CEP-stable, few-cycle pulses with multi- μ J-level energy, at hundreds of kHz repetition rate. Moreover, OPCPAs have extended the range of CEP-stable, ultrashort pulses with moderate energy and high repetition rate towards the mid-IR region³⁶⁻⁴⁰. Some high repetition rate OPCPAs operating at 800 nm have been utilised to generate high-order harmonics with a spectrum in the XUV range showing sensitivity to the value of the CEP of the driving pulse^{9,41}. Krebs et al.⁹ demonstrated a continuous XUV spectrum in the cut-off region using 6.6 fs 918 nm pulses from an OPCPA, suggesting the existence of an isolated pulse in this region of the XUV spectrum. However, the number of XUV photons per pulse was not sufficient to carry out pulse characterisation with the attosecond streaking technique

to determine the temporal structure and pulse duration.

Here we present, to the best of our knowledge, the first demonstration of an attosecond electron streaking experiment driven by XUV pulses operating at 100 kHz repetition rate, i.e. at least an order of magnitude higher than any previous implementation. The ability to do so stems from the available high number of 10^6 XUV photons per pulse on target, which is comparable to typical attosecond light sources driven by post-compressed Ti:Sapphire CPA systems. The temporal structure of the pulse is dominated by a single XUV pulse with sub-140 as duration, demonstrating the suitability of our source for attosecond pump-probe experiments.

A sketch of the experimental setup is shown in Fig. 1. An OPCPA delivered CEP-stable 7 fs pulses at a central wavelength of 790 nm with up to 190 μ J of energy per pulse and at a repetition rate of 100 kHz^{31,42,43}. In HHG the 7 fs pulses from the OPCPA system, containing 2.6 optical cycles, lead to the generation of short APTs containing 7 pulses with varying intensity⁴⁴. To enable efficient amplitude gating of IAPs, the 7 fs OPCPA pulses were compressed to near-single cycle pulse durations, using hollow fibre pulse compression in a 1 m long fibre filled with neon gas in gradient pressure configuration. Spectra spanning more than one octave supporting 3 fs pulses were achieved. Fig. 2 summarises the spatio-temporal characterisation performed with the SEA-F-SPIDER technique⁴⁵, which measures the spatially dependent field in one spatial plane, i.e. either $E(x, y_0, t)$ or $E(x_0, y, t)$. As the non-collinear angle of the OPCPA system lies in the horizontal x -plane, eventual spatio-temporal couplings would be expected in this plane⁴². In Fig. 2(a) the spatio-spectral intensity distribution $|E(\omega, x, y_0)|^2$ is shown. Apart from small spatial variations

(e.g. a frequency-dependent spot size), no significant space-time couplings were observed. In Fig. 2(c) the spatially integrated spectral intensity (red line) and spectral phase (green line) are shown for a series of five measurements acquired over the space of one minute, demonstrating the excellent short term stability of the source. The central wavelength is 760 nm. The spectral phase is flat within the compression range of the chirped mirrors from 500 to 1050 nm and shows small oscillations caused by the chirped mirror compressor. Fig. 2(b) shows the spatio-temporal intensity profile and (d) the spatially integrated temporal intensity. The pulse duration is 3.3 ± 0.1 fs, corresponding to only 1.3 optical cycles. The inset of Fig. 2(d) shows the near-field spatial profile of the beam after the HCF and chirped mirror compressor measured by a CMOS camera.

The near-single-cycle near-infrared (NIR) pulses were sent to an attosecond beamline sketched in Fig. 1 and described in detail in ⁴⁴. The pulses were split with the majority of the pulse energy used for HHG. For this, the near-single-cycle pulses were focused to an approximate intensity of 2×10^{14} W/cm² inside a cylindrical gas cell with a diameter of 2 mm, filled with krypton at a backing pressure of 70 mbar. The optimum CEP was chosen by fine tuning the compression (see **supplementary information**). After HHG the XUV and remaining NIR radiation were separated utilising a dielectric filter mirror and an Al filter. The smaller portion of the NIR energy was used as probe beam. A piezo translation stage in the probe arm was used to provide a variable delay. XUV and NIR pulses were recombined with a holey mirror. Both beams were focused into the experimental chamber by a gold-coated toroidal mirror. The spectrally integrated photon flux on target for the experiment was measured with an XUV photodiode and amounted to 10^6 photons per shot (comparable to typical Ti:Sapphire laser driven attosecond setups), which amounted to an un-

precedented flux of 10^{11} photons per second on target. In the experimental chamber the attosecond XUV pulse ionised neon atoms in the presence of a strong NIR probe pulse ($I \approx 4.6 \text{ TW/cm}^2$) and the resulting photoelectron momentum distributions were measured with a velocity map imaging spectrometer (VMI) ⁴⁶.

For the characterisation of the attosecond XUV pulses the attosecond streaking technique ¹⁰ was employed. Single photon ionisation by the XUV pulses launches a photoelectron wave packet into the continuum. In the absence of the NIR pulse, the photoelectron wave packet reproduces the amplitude and phase of the XUV pulses, re-shaped by the photoionisation cross section, and shifted in energy by the ionisation potential of the target atom. The low photon energy limit of the XUV spectrum, given by the transmission window of the aluminium filter at approximately 15.5 eV lies a few eV below the ionisation threshold of neon (21.56 eV). Therefore, information about the low energy end of the XUV pulse spectrum is lost during photoionisation and the XUV pulse that can be retrieved corresponds to the portion of the spectrum above the ionisation potential of neon. The presence of the NIR pulse modulates the photoelectron kinetic energy distribution depending on the value of the NIR field vector potential at the moment of ionisation giving rise to a streaking effect. Measurements of the photoelectron kinetic energy distribution at a particular observation angle as a function of XUV-NIR delay (i.e., the electron streaking trace) contain amplitude and phase information on both, the NIR and the XUV fields. Within the strong field approximation (SFA), the probability amplitude for producing photoelectrons in the continuum with final momentum \vec{p} is given by ^{10,47,48}:

$$a(\vec{p}, \tau) = -i \int_{-\infty}^{\infty} dt d_{\vec{p}+\vec{A}(t)} E_{\text{XUV}}(t - \tau) e^{i[(W+\text{IP})t - \int_t^{\infty} dt' (\vec{p} \cdot \vec{A}(t') + A(t')^2/2)]} \quad (1)$$

where τ is the time-delay between the NIR and XUV fields, E_{XUV} is the complex amplitude of the electric field of the XUV pulse, $\vec{A}(t)$ is the vector potential of the NIR field, $d_{\vec{p}+\vec{A}(t)}$ is the complex dipole transition matrix element from the ground state to the continuum, IP is the ionisation potential of the ionised atom, $\vec{p} + \vec{A}(t)$ is the instantaneous kinetic momentum, and $W = p^2/2$ is the measured photoelectron kinetic energy. Atomic units are used. The measured electron yield in a streaking trace is proportional to $|a(\vec{p}, \tau)|^2$.

Streaking traces for a range of angles with respect to the polarisation vector were constructed from the measured photoelectron momentum distributions (see **methods** section). Figs. 3 (a)-(d) show the photoelectron kinetic energy distributions as a function of XUV-NIR delay, taken at observation angles of 0° , 15° , 30° , and 45° , respectively. The electron streaking traces clearly show the modulation of the photoelectron kinetic energy distributions as a result of the presence of the NIR field during ionisation. The spectral modulations with an energy spacing of approximately twice the NIR photon energy ω_{NIR} at photon energies below $\approx 20\text{eV}$ indicates the presence of satellite pulses at a delay of $\pm T_{\text{NIR}}/2$ from the main XUV pulse. At the same time, the smooth spectrum above $\approx 20\text{eV}$ kinetic energy suggests that a clean isolated attosecond pulse exists in this portion of the XUV spectrum.

In order to retrieve the XUV and NIR pulses from the experimental trace, most retrieval methods replace the product $\vec{p} \cdot \vec{A}(t)$ in equation (1) by $\vec{p}_o \cdot \vec{A}(t)$, with \vec{p}_o , the central momentum of the kinetic energy distribution. This central momentum approximation (CMA), leads to an over-estimation of the strength of the streaking effect at low kinetic energies. Validity of the CMA

requires the central momentum of the kinetic energy distribution to be considerably larger than its bandwidth ($|\vec{p}_o| \gg \Delta p$), a condition that is certainly not met in the measurements shown in Fig. 3. Therefore, the Volkov-transform generalized projection algorithm (VTGPA) ⁴⁹ was chosen as retrieval method to analyse the experimental data. The VTGPA method determines an explicit solution for $E_{\text{XUV}}(t)$ by finding a local minimum of an error function (or a figure of merit expression) ⁴⁹. If the error function for a particular streaking trace contains many local minima, the solution of the VTGPA may converge to any of those minima. Therefore, to complement the analysis of our data sets by the VTGPA, an alternative method was developed, based on a global optimisation routine. This method, which we call streaking global optimisation (SGO) guesses the XUV spectrum from a weakly streaked region of the experimental trace, and utilises equation (1) and standard global optimisation routines to fit the spectral phase. The attosecond pulse retrieval algorithms and the data processing are discussed in detail in the **supplementary information**.

Note that equation (1) assumes that the effect of the attractive Coulomb field on the escaping photoelectron can be neglected, and furthermore, that the only ionisation pathway is single photon ionisation by the XUV field. As a result of the second assumption and due to the phase term $\vec{p} \cdot \vec{A}(t)$, it is expected that electron streaking traces at different observation angles differ in the strength of the streaking effect, as observed in the traces shown in Figs. 3 (a) to (d). Additional differences in the shape of the photoelectron spectra arise due to the angle-dependence of the dipole transition matrix element. In Figs. 3 (a) to (d) the relative spectral amplitude at lower photoelectron energies increases with angle. In addition, inspection of the energy-integrated electron yield as a function of the XUV-NIR delay shows a strong modulation of the yield in the regions where the streaking

field is strongest. This modulation has an opposite sign in the top and bottom portions of the streaking trace. Due to the strong NIR field and very short pulse duration one can expect a high degree of ground state polarisation by the strong NIR field, which in turn strongly changes the photoionisation probability.

In order to assess the validity of the VTGPA and the SGO in the presence of the aforementioned effects in the experimental data, the algorithms were first applied to simulated streaking traces, that were obtained by numerically solving the time-dependent Schrödinger equation (TDSE) in the single-active electron approximation, with an effective potential for neon⁵⁰. Analysis of the simulated results shows that both methods are able to satisfactorily retrieve the input XUV field with a relative pulse field error for normalised fields⁵¹ on the order of 0.1. Further details can be found in the **supplementary information**.

The VTGPA and SGO methods were applied to a set of experimental traces at different observation angles. In total, 32 different experimental traces were analysed with each retrieval method. More details about the data processing and the analysis are presented in the **supplementary information**. Fig. 4 shows a summary of the results. Figs. 4 (a) and (c) show the absolute value squared of the average XUV pulse envelope retrieved with the VTGPA and the SGO algorithms, respectively. A confidence region of $\pm 1\sigma$ is indicated by the light blue shaded area, which is not visible on a linear scale. The pulse retrievals by the VTGPA result in an average pulse duration of 132 ± 5 as FWHM, while the SGO algorithm retrieves XUV pulses with a FWHM of 124 ± 3 as. The insets in (a) and (c) show the temporal intensity profiles on a logarithmic scale. The pre-pulse

satellite located at ≈ -1.35 fs (approximately one half of the NIR laser period) has a relative intensity of 0.7×10^{-3} , and 1.0×10^{-3} for the VTGPA and SGO retrievals respectively. The post-pulse satellite located at $\approx +1.35$ fs has a relative intensity of 4×10^{-4} , and 6×10^{-4} for the VTGPA and SGO retrievals respectively. The satellite pre- and post-pulses stem from XUV emission from the two weaker neighbouring half-cycles of the NIR field and are not unexpected for purely amplitude gated HHG. Their extremely low relative intensity underscores the usefulness of our source for attosecond pump-probe experiments. Figs. 4 (b) and (d) show the retrieval results in the spectral domain. The mean of the retrieved spectral intensities is plotted as a dark green line with the confidence region of $\pm 1\sigma$ indicated by the light green shaded area. Similarly, the means of the spectral phases are plotted as dark red dashed lines, with the $\pm 1\sigma$ confidence intervals as light red shaded areas. In both cases the phases are essentially flat with a residual negative third order component, as is expected for XUV pulses near the cut-off region with phase-matching favouring the short trajectories⁵². Individual reconstructed streaking traces are shown in the **supplementary information**.

In summary, we have demonstrated the generation and characterisation of high flux isolated attosecond XUV pulses at an unprecedented repetition rate of 100 kHz. This was achieved by direct amplitude gating of HHG using near-single-cycle (3.3 fs) driving pulses obtained by hollow fibre compression of pulses from an OPCPA laser system. The high XUV photon flux of our source allowed performing attosecond electron streaking experiments. The measured streaking traces clearly indicate the presence of isolated XUV pulses, which have been retrieved utilising two different retrieval algorithms, previously tested by analysing simulated streaking traces generated

by numerically solving the time-dependent Schrödinger equation. It is envisioned that this high repetition rate source of attosecond pulses will enable attosecond pump-probe spectroscopy studies with electron-ion coincidence detection, allowing data collection speeds one order of magnitude higher than currently operating systems.

Methods

High repetition rate near single-cycle laser. The pulses from the OPCPA system^{31,42,43} were sent into a 1 m long 340 μm diameter hollow-core fibre (HCF). The HCF was operated in differential pumping configuration^{45,53,54}, i.e. the entrance side was kept at a $\approx 1 \times 10^{-1}$ mbar vacuum, whilst the exit volume was filled with neon gas at a pressure of 2.5 bar. Dispersion compensation was achieved using chirped mirrors (Ultrafast Innovations, PC70) with a negative group delay dispersion in the range of 500 to 1050 nm. A pair of ultra-thin fused silica wedges was employed for fine tuning of the dispersion to achieve optimal compression inside the HHG target. The pulse energy after losses in the chirped mirror compressor and the ultra-thin wedges was 95 μJ .

Streaking traces. For each delay between the XUV and NIR pulses, a VMI image was acquired with an integration time of approximately 15 seconds. Three-dimensional momentum distributions were retrieved from the experimental images by applying an Abel inversion⁵⁵ based on the rBASEX algorithm^{56,57}. This results in angular distributions described by an expansion in terms of Legendre polynomials. Legendre terms up to order 14 were used to account for the maximum number of photons involved in the strong NIR field dressed photoionisation process. The Legendre expansion allows building streaking traces at any particular angle with respect to the polarisation

axis. For further analysis, streaking traces at angles of 0, 15, 30, 45, 135, 150, 165, and 180 degrees with respect to the laser polarisation axis were constructed. A separate experimental image of photoionisation of neon by harmonics produced with narrowband XUV pulses obtained by evacuating the hollow fibre was used to calibrate the kinetic energy axis of the VMI spectrometer.

1. Krausz, F. & Ivanov, M. Attosecond physics. *Rev. Mod. Phys.* **81**, 163 (2009). URL <http://link.aps.org/abstract/RMP/v81/p163>.
2. Hentschel, M. *et al.* Attosecond metrology. *Nature* **414**, 509–513 (2001). URL <https://www.nature.com/articles/35107000>.
3. Krausz, F. & Stockman, M. I. Attosecond metrology: from electron capture to future signal processing. *Nature Photonics* **8**, 205–213 (2014). URL <https://www.nature.com/articles/nphoton.2014.28>.
4. Lépine, F., Ivanov, M. Y. & Vrakking, M. J. J. Attosecond molecular dynamics: fact or fiction? *Nature Photonics* **8**, 195–204 (2014). URL <https://www.nature.com/articles/nphoton.2014.25>.
5. Ullrich, J. *et al.* Recoil-ion and electron momentum spectroscopy: reaction-microscopes. *Reports on Progress in Physics* **66**, 1463–1545 (2003). URL <https://doi.org/10.1088/0034-4885/66/9/203>.
6. Boguslavskiy, A. E. *et al.* The Multielectron Ionization Dynamics Underlying Attosecond Strong-Field Spectroscopies. *Science* **335**, 1336–1340 (2012). URL <https://science.sciencemag.org/content/335/6074/1336>. Publisher: American Association for the Advancement of ScienceSection: Report.
7. Cavalieri, A. L. *et al.* Attosecond spectroscopy in condensed matter. *Nature* **449**, 1029–1032 (2007). URL <http://www.nature.com/nature/journal/v449/n7165/abs/nature06229.html>.

8. Chew, S. H. *et al.* Time-of-flight-photoelectron emission microscopy on plasmonic structures using attosecond extreme ultraviolet pulses. *Applied Physics Letters* **100**, 051904 (2012). URL <http://scitation.aip.org/content/aip/journal/apl/100/5/10.1063/1.3670324>.
9. Krebs, M. *et al.* Towards isolated attosecond pulses at megahertz repetition rates. *Nature Photonics Letters* **7**, 555–559 (2013). URL <https://www.nature.com/articles/nphoton.2013.131>.
10. Itatani, J. *et al.* Attosecond streak camera. *Phys. Rev. Lett.* **88**, 173903 (2002). URL <https://link.aps.org/doi/10.1103/PhysRevLett.88.173903>.
11. Ferray, M. *et al.* Multiple-harmonic conversion of 1064 nm radiation in rare gases. *Journal of Physics B: Atomic, Molecular and Optical Physics* **21**, L31–L35 (1988). URL <https://doi.org/10.1088/0953-4075/21/3/001>.
12. Corkum, P., Burnett, N. & Ivanov, M. Subfemtosecond pulses. *Optics Letters* **19**, 1870–1872 (1994). URL <https://doi.org/10.1364/OL.19.001870>.
13. Antoine, P., L’Huillier, A. & Lewenstein, M. Attosecond pulse trains using high-order harmonics. *Phys. Rev. Lett.* **77**, 1234–1237 (1996). URL <https://link.aps.org/doi/10.1103/PhysRevLett.77.1234>.
14. Corkum, P. B. Plasma perspective on strong field multiphoton ionization. *Phys. Rev. Lett.* **71**, 1994–1997 (1993). URL <https://link.aps.org/doi/10.1103/PhysRevLett.71.1994>.

15. Sansone, G. *et al.* Isolated single-cycle attosecond pulses. *Science* **314**, 443–446 (2006). URL <http://science.sciencemag.org/content/314/5798/443>.
16. Kim, K. T. *et al.* Photonic streaking of attosecond pulse trains. *Nature Photonics* **7**, 651–656 (2013). URL <https://www.nature.com/articles/nphoton.2013.170>.
17. Pfeifer, T. *et al.* Generating coherent broadband continuum soft-X-ray radiation by attosecond ionization gating. *Optics Express* **15**, 17120–17128 (2007). URL <http://www.opticsexpress.org/abstract.cfm?URI=oe-15-25-17120>.
18. Uiberacker, M. *et al.* Attosecond real-time observation of electron tunnelling in atoms. *Nature* **446**, 627–632 (2007). URL <https://www.nature.com/articles/nature05648>.
19. Goulielmakis, E. *et al.* Real-time observation of valence electron motion. *Nature* **466**, 739–743 (2010). URL <http://www.nature.com/nature/journal/v466/n7307/abs/nature09212.html>.
20. Sansone, G. *et al.* Electron localization following attosecond molecular photoionization. *Nature* **465**, 763–766 (2010). URL <http://www.nature.com/nature/journal/v465/n7299/abs/nature09084.html>.
21. Nisoli, M. *et al.* Compression of high-energy laser pulses below 5 fs. *Opt. Lett.* **22**, 522–524 (1997). URL <http://ol.osa.org/abstract.cfm?URI=ol-22-8-522>.
22. Sabbar, M. *et al.* Combining attosecond XUV pulses with coincidence spectroscopy. *Review of Scientific Instruments* **85**, 103113 (2014). URL <http://aip.scitation.org/doi/abs/10.1063/1.4898017>.

23. Cattaneo, L. *et al.* Attosecond coupled electron and nuclear dynamics in dissociative ionization of H₂. *Nature Physics* **1** (2018). URL <https://www.nature.com/articles/s41567-018-0103-2>.
24. Vos, J. *et al.* Orientation-dependent stereo Wigner time delay and electron localization in a small molecule. *Science* **360**, 1326–1330 (2018). URL <http://science.sciencemag.org/content/360/6395/1326>.
25. Stockman, M. I., Kling, M. F., Kleineberg, U. & Krausz, F. Attosecond nanoplasmonic-field microscope. *Nature Photonics* **1**, 539–544 (2007). URL <https://www.nature.com/articles/nphoton.2007.169>.
26. Okell, W. A. *et al.* Temporal broadening of attosecond photoelectron wavepackets from solid surfaces. *Optica* **2**, 383–387 (2015). URL <http://www.opticsinfobase.org/optica/abstract.cfm?URI=optica-2-4-383>.
27. Furch, F. J. *et al.* Close to transform-limited, few-cycle 12 μJ pulses at 400 kHz for applications in ultrafast spectroscopy. *Opt. Express* **24**, 19293–19310 (2016). URL <http://www.opticsexpress.org/abstract.cfm?URI=oe-24-17-19293>.
28. Rothhardt, J., Demmler, S., Hädrich, S., Limpert, J. & Tünnermann, A. Octave-spanning OPCPA system delivering CEP-stable few-cycle pulses and 22 W of average power at 1 MHz repetition rate. *Opt. Express* **20**, 10870–10878 (2012). URL <http://www.opticsexpress.org/abstract.cfm?URI=oe-20-10-10870>.

29. Prinz, S. *et al.* CEP-stable, sub-6 fs, 300-kHz OPCPA system with more than 15 W of average power. *Opt. Express* **23**, 1388–1394 (2015). URL <http://www.opticsexpress.org/abstract.cfm?URI=oe-23-2-1388>.
30. Matyschok, J. *et al.* Temporal and spatial effects inside a compact and CEP stabilized, few-cycle OPCPA system at high repetition rates. *Opt. Express* **21**, 29656–29665 (2013). URL <http://www.opticsexpress.org/abstract.cfm?URI=oe-21-24-29656>.
31. Furch, F. J. *et al.* CEP-stable few-cycle pulses with more than 190 μJ of energy at 100 kHz from a noncollinear optical parametric amplifier. *Optics Letters* **42**, 2495–2498 (2017). URL <https://www.osapublishing.org/abstract.cfm?uri=ol-42-13-2495>.
32. Hrisafov, S. *et al.* High-power few-cycle near-infrared OPCPA for soft X-ray generation at 100 kHz. *Opt. Express* **28**, 40145–40154 (2020). URL <http://www.opticsexpress.org/abstract.cfm?URI=oe-28-26-40145>.
33. Lavenu, L. *et al.* High-power two-cycle ultrafast source based on hybrid nonlinear compression. *Optics Express* **27**, 1958–1967 (2019). URL <https://www.osapublishing.org/oe/abstract.cfm?uri=oe-27-3-1958>. Publisher: Optical Society of America.
34. Hädrich, S. *et al.* 500 W, 5 mJ, 6 fs, CEP-stable few-cycle pulses: An update on the ELI-ALPS HR2 beamline (Conference Presentation). In Dong, L. (ed.) *Fiber Lasers XVII: Technology and Systems*, vol. 11260. International Society for Optics and Photonics (SPIE, 2020). URL <https://doi.org/10.1117/12.2544603>.

35. Müller, M. *et al.* Multipass cell for high-power few-cycle compression. *Optics Letters* **46**, 2678–2681 (2021). URL <https://www.osapublishing.org/ol/abstract.cfm?uri=ol-46-11-2678>. Publisher: Optical Society of America.
36. Pupeikis, J. *et al.* Water window soft X-ray source enabled by a 25 W few-cycle 2.2 μm OPCPA at 100 kHz. *Optica* **7**, 168–171 (2020). URL <http://www.osapublishing.org/optica/abstract.cfm?URI=optica-7-2-168>.
37. Thiré, N. *et al.* Highly stable, 15 W, few-cycle, 65 mrad CEP-noise mid-IR OPCPA for statistical physics. *Opt. Express* **26**, 26907–26915 (2018). URL <http://www.opticsexpress.org/abstract.cfm?URI=oe-26-21-26907>.
38. Neuhaus, M. *et al.* 10 W CEP-stable few-cycle source at 2 μm with 100 kHz repetition rate. *Opt. Express* **26**, 16074–16085 (2018). URL <http://www.opticsexpress.org/abstract.cfm?URI=oe-26-13-16074>.
39. Elu, U. *et al.* High average power and single-cycle pulses from a mid-IR optical parametric chirped pulse amplifier. *Optica* **4**, 1024–1029 (2017). URL <http://www.osapublishing.org/optica/abstract.cfm?URI=optica-4-9-1024>.
40. Mero, M. *et al.* 43 W, 1.55 μm and 12.5 W, 3.1 μm dual-beam, sub-10 cycle, 100 kHz optical parametric chirped pulse amplifier. *Opt. Lett.* **43**, 5246–5249 (2018). URL <http://ol.osa.org/abstract.cfm?URI=ol-43-21-5246>.
41. Harth, A. *et al.* Compact 200 kHz HHG source driven by a few-cycle OPCPA. *Journal of Optics* **20**, 014007 (2017).

42. Witting, T., Furch, F. J. & Vrakking, M. J. Spatio-temporal characterisation of a 100 kHz 24 W sub-3-cycle NOPCPA laser system. *Journal of Optics* **20**, 044003 (2018). URL <http://stacks.iop.org/2040-8986/20/i=4/a=044003>.
43. Hoff, D. *et al.* Continuous every-single-shot carrier-envelope phase measurement and control at 100 kHz. *Opt. Lett.* **43**, 3850–3853 (2018). URL <http://ol.osa.org/abstract.cfm?URI=ol-43-16-3850>.
44. Osolodkov, M. *et al.* Generation and characterisation of few-pulse attosecond pulse trains at 100 kHz repetition rate. *Journal of Physics B: Atomic, Molecular and Optical Physics* **53**, 194003 (2020). URL <https://iopscience.iop.org/article/10.1088/1361-6455/aba77d>. Publisher: IOP Publishing.
45. Witting, T. *et al.* Characterization of high-intensity sub-4-fs laser pulses using spatially encoded spectral shearing interferometry. *Optics Letters* **36**, 1680–2 (2011). URL <http://www.opticsinfobase.org/ol/abstract.cfm?uri=ol-36-9-1680>.
46. Ghafur, O. *et al.* A velocity map imaging detector with an integrated gas injection system. *Review of Scientific Instruments* **80**, 033110 (2009). URL <https://aip.scitation.org/doi/full/10.1063/1.3085799>.
47. Lewenstein, M., Balcou, P., Ivanov, M. Y., L’Huillier, A. & Corkum, P. B. Theory of high-harmonic generation by low-frequency laser fields. *Phys. Rev. A* **49**, 2117–2132 (1994). URL <https://link.aps.org/doi/10.1103/PhysRevA.49.2117>.

48. Mairesse, Y., & Quere, F. Frequency-resolved optical gating for complete reconstruction of attosecond bursts. *Physical Review A* **71**, 011401 (2005). URL <http://link.aps.org/doi/10.1103/PhysRevA.71.011401>.
49. Keathley, P. D., Bhardwaj, S., Moses, J., Laurent, G. & Kärtner, F. X. Volkov transform generalized projection algorithm for attosecond pulse characterization. *New J. Phys.* **18**, 073009 (2016). URL <http://stacks.iop.org/1367-2630/18/i=7/a=073009>.
50. Patchkovskii, S., Vrakking, M. J. J., Villeneuve, D. M. & Niikura, H. Selection of the magnetic quantum number in resonant ionization of neon using an XUV-IR two-color laser field. *J. Phys. B* 134002 (2020). URL <https://iopscience.iop.org/article/10.1088/1361-6455/ab82e0>.
51. Dorrer, C. & Walmsley, I. A. Accuracy criterion for ultrashort pulse characterization techniques: application to spectral phase interferometry for direct electric field reconstruction. *J. Opt. Soc. Am. B* **19**, 1019–1029 (2002). URL <https://doi.org/10.1364/JOSAB.19.001019>.
52. Varjú, K., Johnsson, P., Mauritsson, J., L’Huillier, A. & López-Martens, R. Physics of attosecond pulses produced via high harmonic generation. *American Journal of Physics* **77**, 389 (2009). URL <https://aapt.scitation.org/doi/10.1119/1.3086028>.
53. Suda, A., Hatayama, M., Nagasaka, K. & Midorikawa, K. Generation of sub-10-fs, 5-mJ-optical pulses using a hollow fiber with a pressure gradient. *Applied Physics Letters* **86**, 111116 (2005). URL <https://aip.scitation.org/doi/10.1063/1.1883706>.

54. Okell, W. A. *et al.* Carrier-envelope phase stability of hollow fibers used for high-energy few-cycle pulse generation. *Optics Letters* **38**, 3918–3921 (2013). URL <http://ol.osa.org/abstract.cfm?URI=ol-38-19-3918>.
55. Hickstein, D. D., Gibson, S. T., Yurchak, R., Das, D. D. & Ryazanov, M. A direct comparison of high-speed methods for the numerical Abel transform. *Review of Scientific Instruments* **90**, 065115 (2019). URL <https://aip.scitation.org/doi/10.1063/1.5092635>.
56. Ryazanov, M. *Development and implementation of methods for sliced velocity map imaging. Studies of overtone-induced dissociation and isomerization dynamics of hydroxymethyl radical (CH₂OH and CD₂OH)*. Ph.D. thesis, University of Southern California, Los Angeles (2012). URL <https://digitallibrary.usc.edu/asset-management/2A3BF169XWB4>.
57. Ryazanov, M. & Reisler, H. Improved sliced velocity map imaging apparatus optimized for H photofragments. *The Journal of Chemical Physics* **138**, 144201 (2013). URL <https://aip.scitation.org/doi/10.1063/1.4798929>. Publisher: American Institute of Physics.

Acknowledgements This work was supported financially by the European Union Horizon 2020 Marie Curie ITN project ASPIRE (674960). C.S.M. acknowledges support of grant DoD ONR N00014-17-1-2536. The authors thank R. Peslin, A. Loudovici, and Ch. Reiter for technical support.

Author contributions T.W., M.O., F.S., P.S., C.P.S, and F.J.F. built the experimental setup. F.C. and C.S.M. designed and manufactured the XUV filtering mirror. T.W., M.O., and F.J.F. performed the exper-

iments. T.W. and F.J.F. analysed the data. F.M. and S.P. performed the numerical simulations. T.W. and F.J.F. wrote the manuscript with contributions from M.O., F.M., C.P.S., and M.J.J.V. All authors discussed the results and the analysis of the data.

Additional Information Correspondence and requests for materials should be addressed to T.W. or F.J.F

Competing Interests The authors declare no competing financial interests.

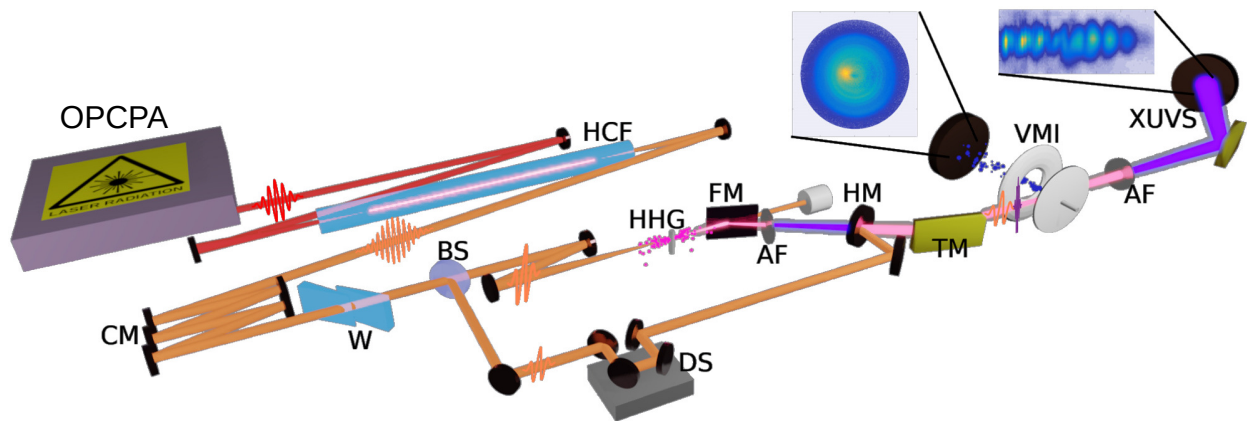


Fig. 1 | Schematic view of the experimental setup. Pulses from an OPCPA laser system are compressed in a hollow-core fibre (HCF). The pulses are split by a beam splitter (BS). HHG takes place in one arm of the interferometer. The pulses are recombined with a variable delay and focused into the velocity map imaging spectrometer (VMI). CM: Chirped mirrors; W: fused silica wedges; DS: delay stage; FM: filter mirror; AF: aluminium filter; HM: holey mirror; TM: toroidal mirror; XUVS: XUV spectrometer.

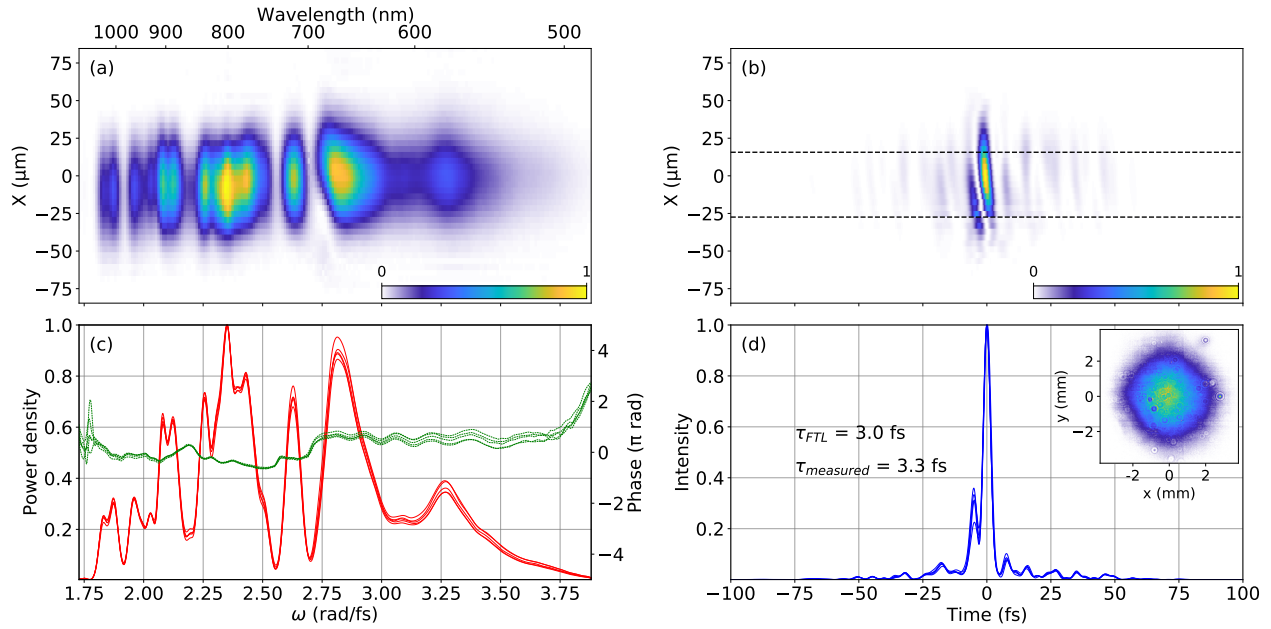


Fig. 2 | Spatio-temporal characterisation of the near-single cycle pulses. (a) Spatio-spectral intensity distribution $|E(x, y_0, \omega)|^2$. (b) Spatio-temporal intensity distribution $|E(x, y_0, t)|^2$. (c) Spatially integrated spectral intensity (red line), and spatially integrated spectral phase (green line). Results from 5 consecutive measurements are shown. (d) Spatially integrated temporal intensity profile (blue line); results from 5 consecutive measurements are plotted. The inset in (d) shows the spatial near-field beam profile on a CMOS camera.

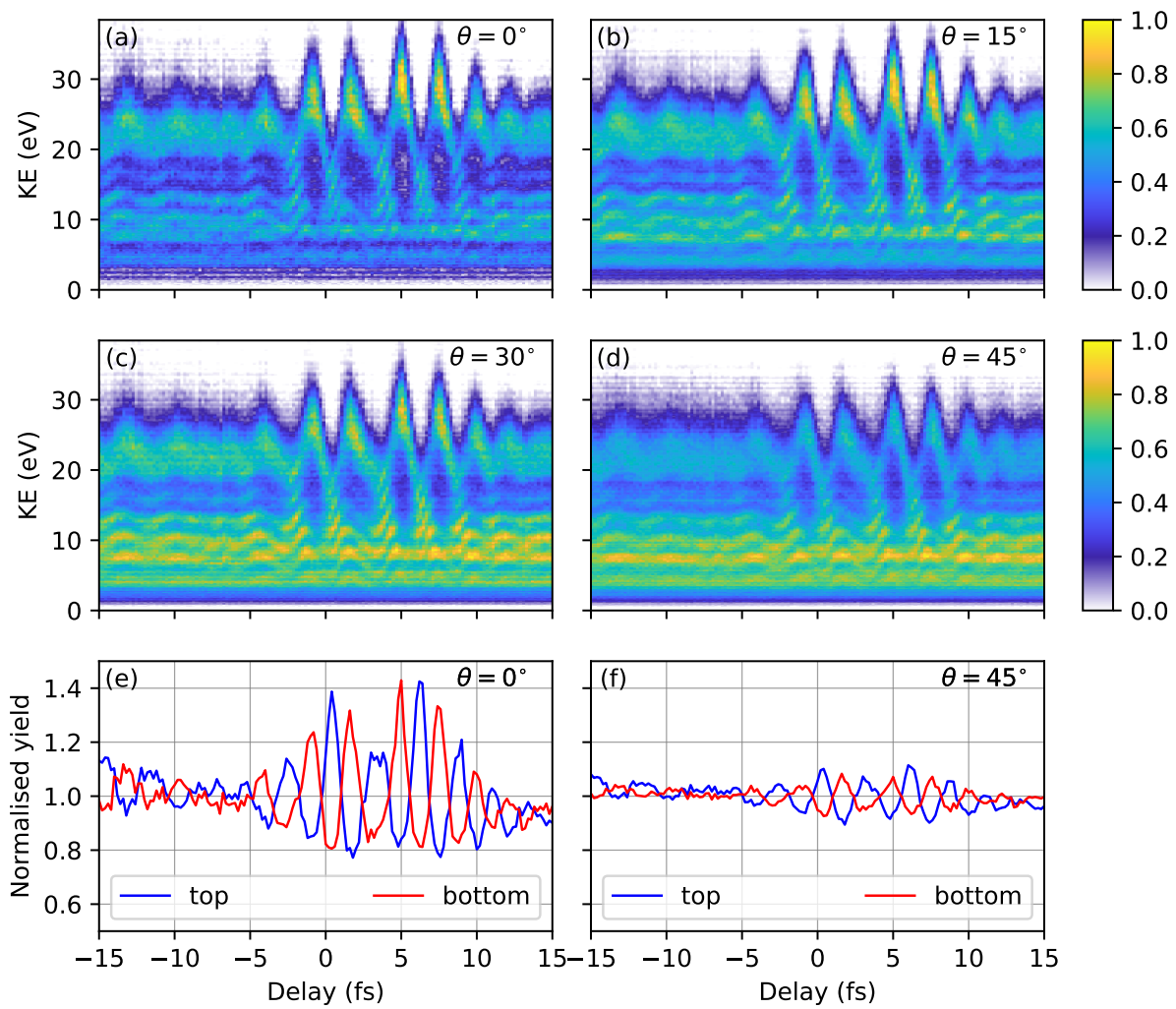


Fig. 3 | Attosecond electron streaking traces. Streaking traces from photoelectron kinetic energy distributions at different observation angles θ with respect to the laser polarisation. (a) $\theta = 0^\circ$, (b) $\theta = 15^\circ$, (c) $\theta = 30^\circ$, and (d) $\theta = 45^\circ$. In all cases the colour scale indicates the electron yield and it is normalised to the maximum of the trace. (e) and (f) show normalised electron yields as a function of delay for observation angles of 0° and 45° respectively, and computed in the top and bottom parts of the detector.

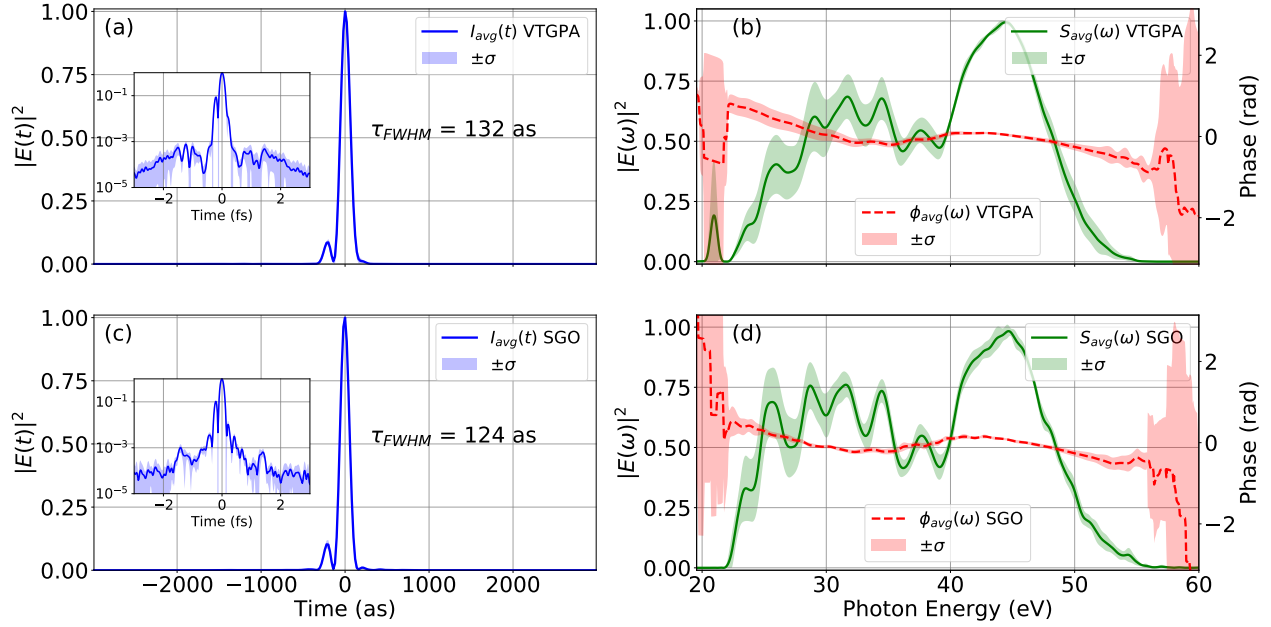


Fig. 4 | Retrieval of the XUV IAPs. (a) Retrieved XUV pulse intensity envelope normalised to its maximum value. The blue line corresponds to the average over all VTGPA retrievals and the shaded area corresponds to 1 standard deviation around the mean (not visible on the linear scale). The inset shows the intensity envelope on a logarithmic scale. (b) Retrieved average spectrum (green) and spectral phase (red dashed line) corresponding to the pulse in (a). The shaded areas correspond to 1 standard deviation around the means. (c) and (d) show the corresponding results found with the SGO retrievals.

Supplementary Information for: Generation and characterisation of isolated attosecond pulses at 100 kHz repetition rate

Tobias Witting^{1,*}, Mikhail Osolodkov¹, Felix Schell¹, Felipe Morales¹, Serguei Patchkovskii¹, Peter Šušnjar¹, Fabio Cavalcante², Carmen S. Menoni², Claus P. Schulz¹, Federico J. Furch^{1,†} and Marc J. J. Vrakking¹

¹*Max Born Institute for Nonlinear Optics and Short Pulse Spectroscopy, Max-Born-Strasse 2a, 12489 Berlin, Germany*

²*Department of Electrical and Computer Engineering, Colorado State University, Fort Collins, CO 80523, USA*

**email: tobias.witting@mbi-berlin.de*

†email: furch@mbi-berlin.de

S1 Optimisation of the NIR pulse duration and the CEP

In order to optimise the NIR pulse duration and to find the optimum CEP for efficient gating of one attosecond pulse a wedge scan was performed. The amount of fused silica inserted into the path of the NIR beam was controlled with a pair of thin fused-silica wedges mounted on linear stages. Fig. S1 shows measured HHG spectra as a function of the glass insertion (top) and an integration over the spectral coordinate (bottom). From the spectrally integrated data the optimum pulse compression for which the XUV emission reaches a maximum cut-off can be determined.

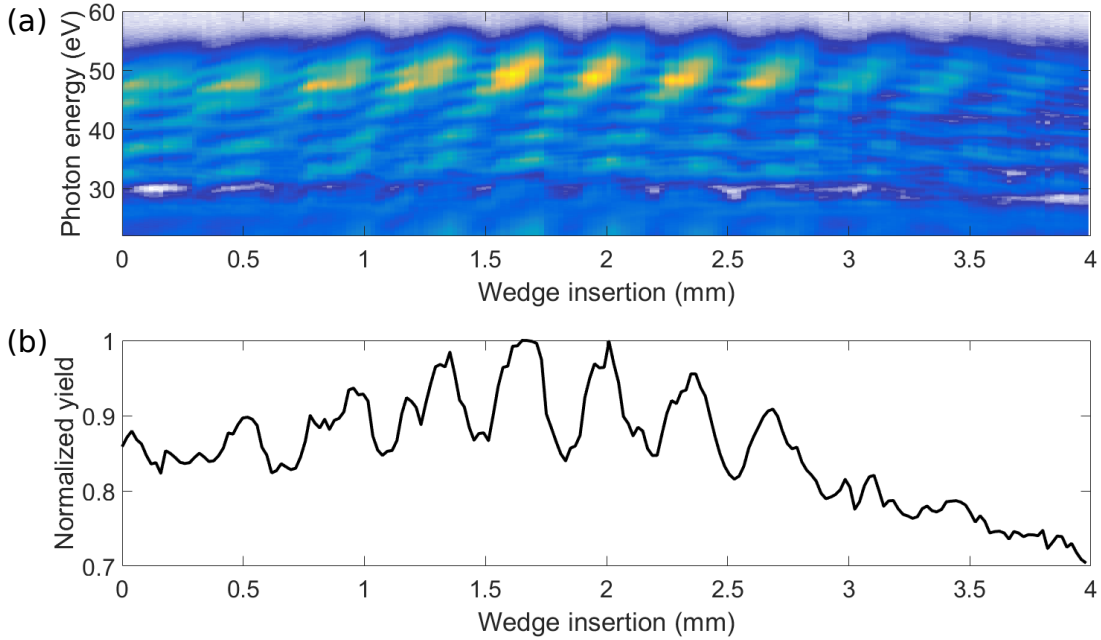


Fig. S1 | Wedge insertion scan for NIR pulse duration optimisation and CEP fine-tuning. (a) XUV spectra as a function of thin-wedge insertion into the NIR beam path. (b) Normalized XUV photon yield as function of the wedge insertion.

Around this maximum in XUV cut-off, the wedge position was fine-tuned to find the optimum CEP which minimises the spectral modulation at high photon energy, which in turn is an indication for isolated attosecond pulses[?].

S2 Attosecond pulse retrieval algorithms

In our implementation of the VTGPA, a first guess of the temporal shape of the vector potential $\vec{A}(t)$ was extracted directly from the experimental streaking trace by integrating the data over the kinetic energy axis for energies above 14 eV, while the initial amplitude was set to 5 TW/cm².

The amplitude of the vector potential was a fit-parameter during the successive iterations. The algorithm completed 250 iterations or was terminated when the figure of merit ϵ_{trace} (defined in (S1) below) of the fit had a relative change from one iteration to the next below 5×10^{-5} . The algorithm was initialised with an XUV spectrum guessed from the experimental trace, based on a weakly streaked region of the trace, and corrected with the energy-dependent cross section of single photon ionization of neon.

In the SGO method, the initial guess of the NIR pulse and the XUV spectrum was generated in the same way as in our implementation of the VTGPA. The XUV spectral phase was parametrised by 70 points equidistant on the frequency axis, in the region where the XUV spectrum was non-zero ($\approx 21 \text{ eV} - 55 \text{ eV}$). Subsequently, a cubic spline interpolation was performed to build the spectral phase on the same frequency axis as the XUV spectrum. Upon a Fourier transform, the XUV field in the time domain and the guessed NIR pulse were used to calculate a guessed streaking trace according to eq. (1) of the main manuscript. This calculated trace was compared to the experimental trace in order to obtain an error or figure of merit according to:

$$\epsilon_{\text{trace}} = \frac{\sum_{i,j} |ST[i,j] - RT[i,j]|}{\sum_{i,j} ST[i,j]} \quad (\text{S1})$$

where $ST[i,j]$ and $RT[i,j]$ are two-dimensional arrays representing the measured streaking trace and the reconstructed streaking trace utilising the guessed pulses, respectively. The 71 resulting parameters (70 for the XUV spectral phase, 1 for the NIR amplitude) were fit while minimising the error function utilising standard global optimisation routines from the scipy python package. In particular the basin-hopping algorithm[?] (50 iterations) was used in order to reach a global solution.

Beyond the points discussed in the previous section, a remaining challenge in the retrieval process is systemic to all spectrographic pulse retrieval methods^{?,?,?}. The phase of the unknown pulse is encoded in amplitudes of the measured trace; e.g. for an unknown pulse with a satellite, the traces corresponding to slight changes in the relative phase between main- and satellite pulses are very similar, thus leading to comparable values of ϵ_{trace} . As a result, the algorithms tend to stagnate in local minima of the error function ϵ_{trace} .

S3 Attosecond pulse retrievals from simulated traces

In this section, numerical simulations are utilised to evaluate the performance of the retrieval algorithms. Neither the Volkov-transform generalised projection algorithm (VTGPA)⁴⁹ nor the streaking global optimisation (SGO) take into account the effect of the Coulomb field on the slower photoelectrons, contributions to the electron yield from ionised excited states, higher order processes in the two-colour photoionisation process. All these processes can alter the observed photoelectron spectra and therefore the streaking trace, but are not taken into account by the SFA description underlying both the VTGPA, and SGO algorithms.

Fig. S2 (a) shows a calculated streaking trace taking into account only photoelectrons emitted at 0° with respect to the laser polarisation. Details about the numerical simulations are discussed below. In Fig. S2 (b) the photoelectron yield integrated over the kinetic energy axis in Fig. S2 (a) is shown. The maxima and minima of the yield coincide with the extrema of the vector potential. The yield modulation is almost 20%. In Fig. S2 (c) the yield over the entire detector (integration

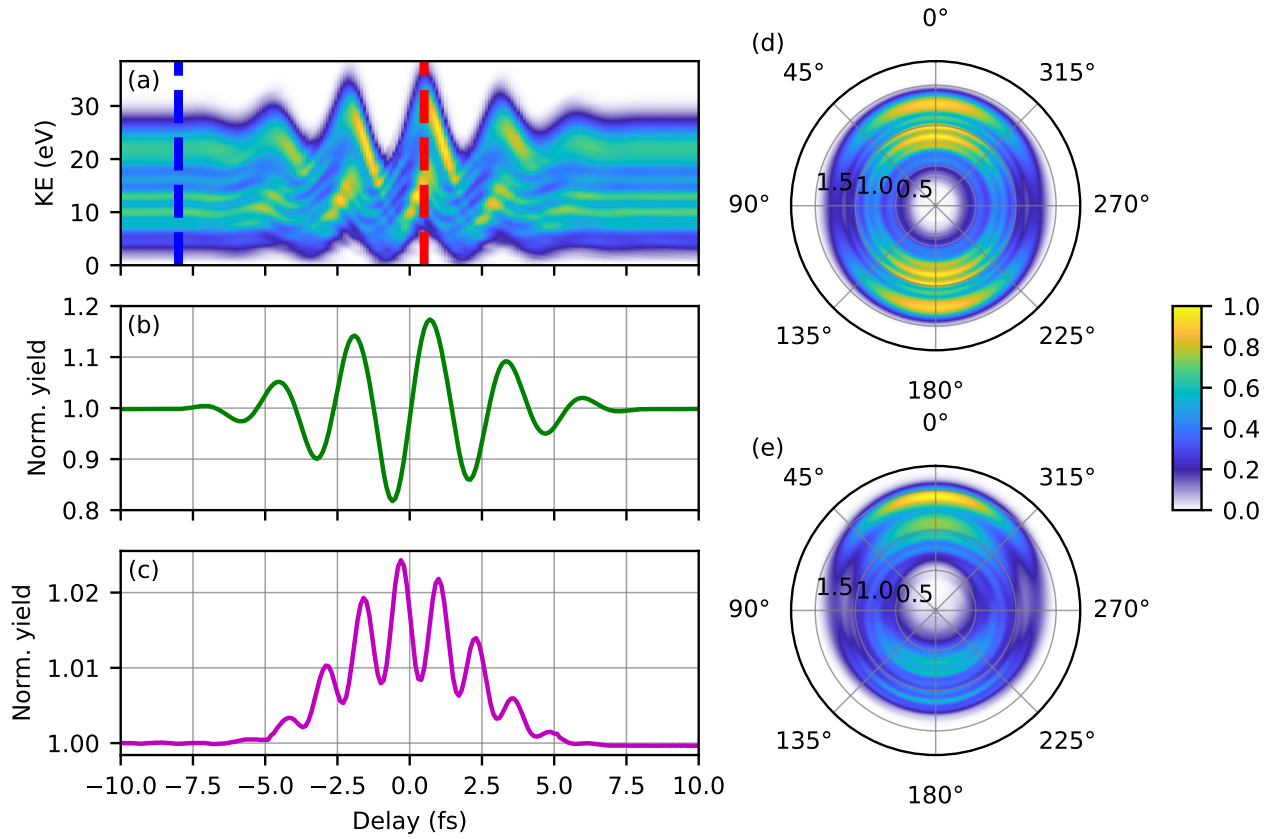


Fig. S2 | Photoelectron yields in the streaking traces. (a) Streaking trace from TDSE calculations; (b) Photoelectron yield calculated by integrating the trace in (a) over the kinetic energy axis; (c) Total yield calculated by integration over the full angular distribution. (d) Photoelectron momentum distribution at zero NIR vector potential (delay position indicated by the blue dashed line in (a)). (e) Photoelectron momentum distribution at large NIR vector potential (delay position indicated by the red dashed line in (a)). The colourbar indicating the normalised photoelectron yield is common to (a), (d), and (e).

over all emission angles) is plotted. Here a yield modulation is also observed, albeit of much smaller magnitude ($\approx 2\%$) and with a $T/2$ periodicity and always increasing with respect to the unstreaked region of the trace. Fig. S2 (d) shows the photoelectron momentum distribution at large delay between NIR and XUV pulses, which represents XUV only photoionisation. In Fig. S2 (e) the momentum distribution is shown, corresponding to a minimum in the amplitude of the vector potential of the NIR field. Here the momentum spheres are shifted along the polarisation axis. Also a change in the yield is observable, with an increased number of photoelectrons emitted in the direction towards which the momentum sphere is shifted. Both the small (Fig. S2 (c)), and the large modulations in the photoelectron yield (Fig. S2 (a), (e)) can be explained by higher order processes in the interaction of the few-cycle strong NIR pulse in combination with the XUV field with the neon target atom. Due to the strong NIR field and very short pulse duration one can expect a high degree of ground state polarisation, which in turn strongly alters the angle-dependent photoionisation probability.

To study the influence of the aforementioned effects on the retrievals, the VTGPA and SGO methods were applied to simulated electron streaking traces. The simulated streaking traces were obtained by solving the time dependent Schrödinger equation (TDSE) using the SCID code, described in [?]. The single active electron neon potential used to describe the different ionisation channels is described in ⁵⁰. The spatial simulation box consisted of 4000 points, with a step-size of 0.05 a.u.. Angular momenta up to $l \leq 40$ were included in the angular part of the wave-function decomposition. In order to avoid reflections from the edges of the simulation box, a complex absorber potential [?] was placed at a distance of $r = 167.3$ a.u. from the origin. The photoelectron spectra for

each of the time delays were calculated using the iSURFV method[?], where the matching distance was set at a distance of $r = 157.3$ a.u. from the origin.

Electron streaking traces at different observation angles were constructed from the angle-resolved photoelectron momentum distributions calculated for varying XUV-NIR delays. In order to recreate conditions similar to the experiment, one pulse retrieved from one experimental data set was utilised as the XUV pulse in the TDSE calculations. The NIR pulse used in the simulations was an 800 nm, 5 fs FWHM transform-limited pulse with a Gaussian envelope and an intensity of 5 TW/cm^2 . Given that the XUV spectrum used for the TDSE simulations is known, the absolute value of the energy- and angle-dependent dipole matrix element that enters equation (1) in the main manuscript can be extracted from XUV-only TDSE results. The dipole term constructed in this way was used for both the retrievals from simulated streaking traces, and the pulse retrievals from experimental data. The phase of the dipole matrix element was ignored, which is a reasonable approximation given that neon has no resonances in the continuum in the spectral region under consideration. A more detailed discussion follows below.

Fig. S3 shows the simulated (left column), retrieved with the VTGPA (center column) and with the SGO (right column) electron streaking traces, at four different observation angles: (a), (b), (c) 0° , (e), (f), (g) 15° , (h), (i), (j) 30° , and (k), (l), (m) 45° . All retrieved traces include the figure of merit ϵ_{trace} . The retrieved traces reproduce most features of the simulated traces qualitatively, apart from a set of barely visible (see Fig S3 (a),(d),(g),(j)) hyperbolic interference fringes at low energy and positive delays, which are the result of the coherent addition of direct ionisation by the

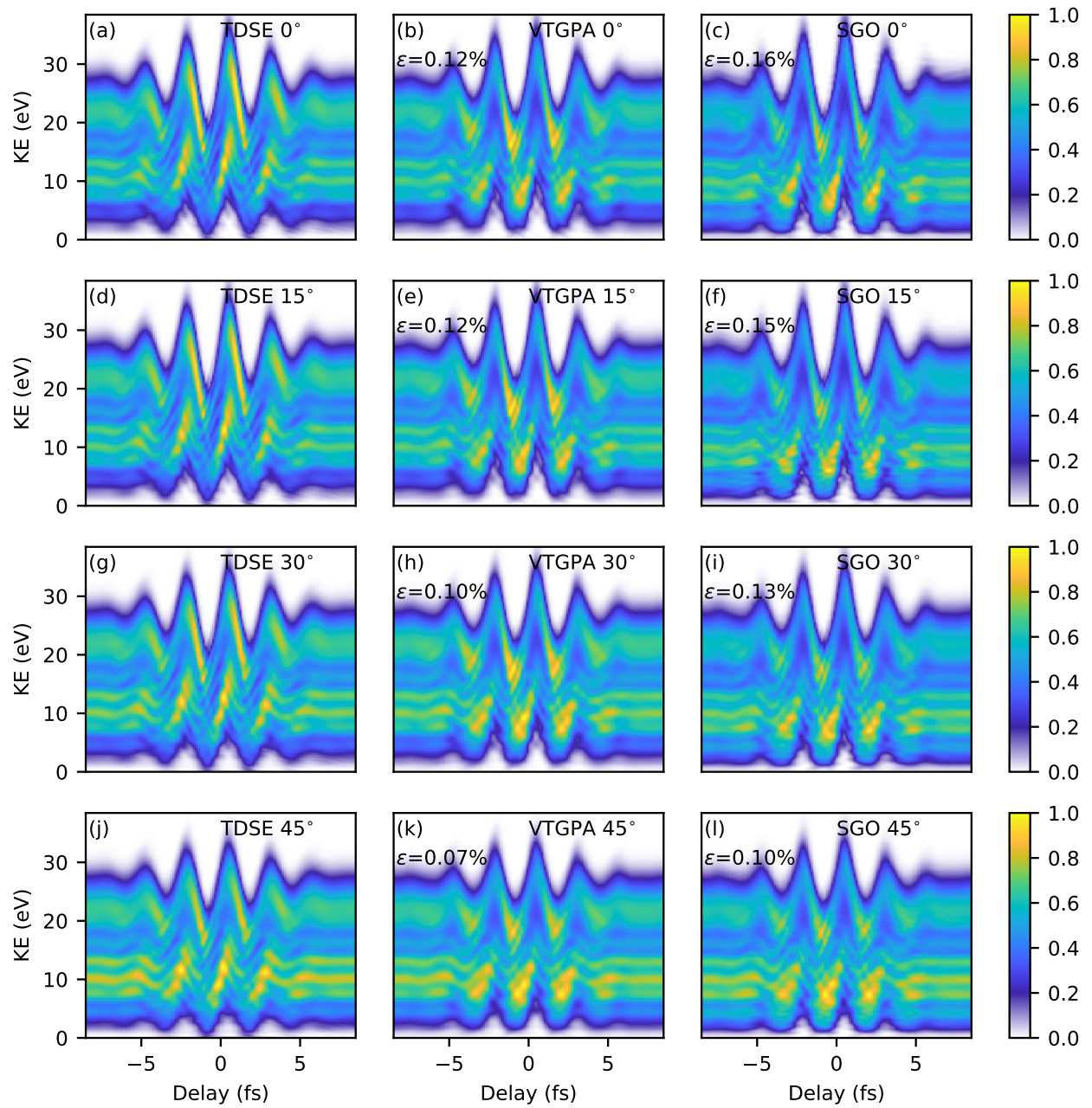


Fig. S3 | Simulated and retrieved streaking traces. Left column: simulated traces at different observation angles; (a) 0° , (e) 15° , (h) 30° and (k) 45° . Center: corresponding reconstructed traces by the VTGPA ((b), (f), (i) and (l) respectively). Right column: corresponding reconstructed traces by the SGO ((c), (g), (j) and (m) respectively).

XUV, and excitation of a bound state by the XUV followed by ionisation by the NIR field[?]. From Fig. S3 one can anticipate that the retrieved NIR intensity has been overestimated by the SGO algorithm. The retrieved intensities for the VTGPA retrievals were 5.0 TW/cm², 5.3 TW/cm², 5.3 TW/cm², and 4.8 TW/cm² for observation angles of 0°, 15°, 30°, and 45° respectively and in the case of the SGO the retrieved intensities were 6.0 TW/cm², 6.0 TW/cm², 6.0 TW/cm², and 5.8 TW/cm². Results of the retrievals with both methods at the previously mentioned four different observation angles, and comparison with the input XUV pulse are presented in Fig. S4. The retrievals with the VTGPA Fig. S4(a) and the SGO Fig. S4(c) methods reproduce the shape of the original XUV pulse very well, including the satellite pulses with intensities around 0.1 % of the maximum intensity. The intensity of the pre-pulse at approximately -1.35 fs is underestimated by an approximate factor of 0.7 in the SGO retrievals, while the VTGPA retrievals on average underestimate the intensity of the pre-pulse by a factor of 0.9. In the case of the post-pulse at approximately 1.35 fs with an intensity of 0.01 % of the maximum, the SGO retrievals overestimate the intensity of the peak on average by a factor of 1.1, while the VTGPA retrievals do not reproduce this peak in the reconstructed temporal pulses. In the experimental data, these satellite pulses would correspond to harmonic generation by the two half-cycles adjacent to the main half-cycle of the NIR driving laser.

The main features of the main pulse are successfully retrieved by both, the VTGPA and the SGO methods. The average retrieved pulse duration (full-width at half maximum of the intensity envelope) by the VTGPA is 140 ± 2 as, compared to the 134 as pulse duration of the pulse used in the TDSE. Meanwhile, the average pulse duration retrieved by the SGO is 136 ± 2 as. The

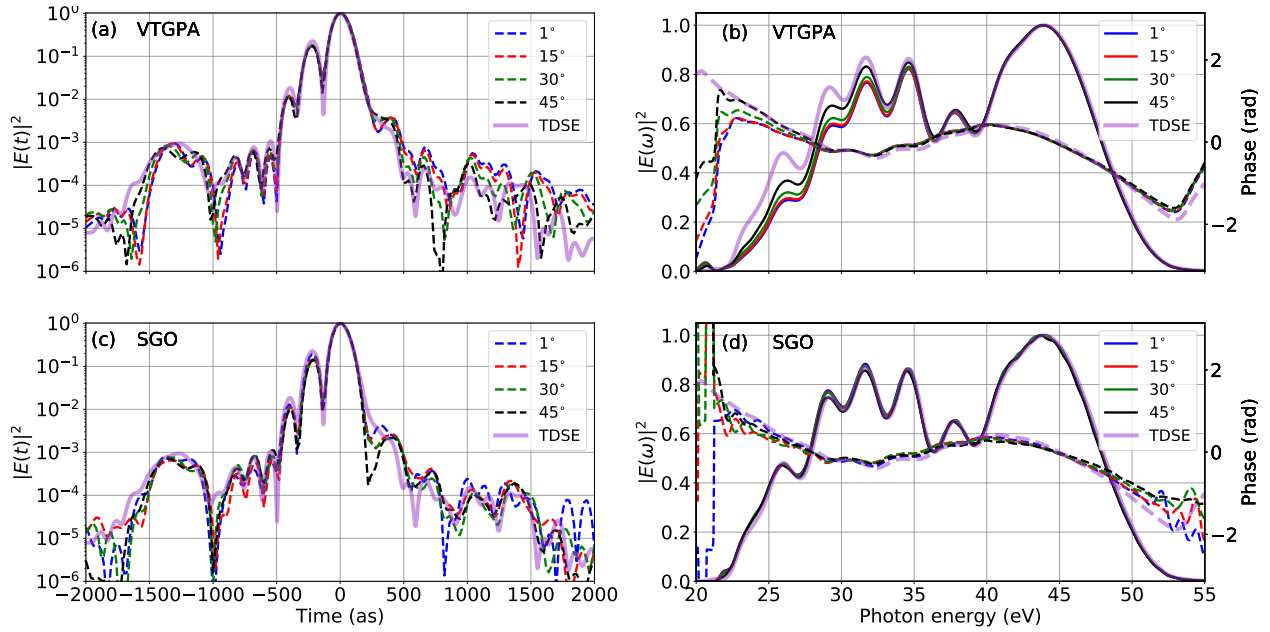


Fig. S4 | Retrieved pulses and spectra from simulated traces. (a) Retrieved pulse temporal shape on logarithmic scale from each retrieval at different observation angles with the VTGPA method in comparison with the original input pulse. (b) Corresponding spectra and spectral phases. (c) and (d) show the retrieved pulses in time and frequency domains respectively for the retrievals performed with the SGO method.

shoulder on the leading edge of the main pulse due to a third-order term in the spectral phase is well reproduced for all retrievals, although both algorithms seem to slightly underestimate the magnitude of the third order dispersion. This is also observable in the spectral domain plot. Based on the simulations we conclude that the retrieved pulses reproduce the original pulse with high fidelity down to intensities of 0.1 % of the maximum.

In order to quantify the differences between the retrieved and original pulses, the root-mean-square field (RMSF) error defined by Dorrer and Walmsley ⁵¹ was determined for all retrievals.

The RMSF error is defined according to:

$$\epsilon_{\text{RMSF}} = \int_{-\infty}^{+\infty} |E_{\text{TDSE}}(t) - E_{\text{ret}}(t)|^2 dt, \quad (\text{S2})$$

where $E_{\text{TDSE}}(t)$ is the input XUV pulse used in the TDSE calculations and $E_{\text{ret}}(t)$ is the pulse retrieved either by the VTGPA or the SGO method. In order to compute a dimensionless quantity both fields are normalized according to:

$$E_{\text{normalized}} = \frac{E(t)}{\int_{-\infty}^{+\infty} |E(t)|^2 dt} \quad (\text{S3})$$

The RMSF error defined in this way varies between 0 and 2, where a number $\lesssim 0.1$ is considered to be an adequate pulse retrieval. The calculated RMSF errors were 1.43×10^{-1} , 1.39×10^{-1} , 1.16×10^{-1} , and 0.87×10^{-1} for the VTGPA results at observation angles of 0° , 15° , 30° , and 45° respectively. Meanwhile, the calculated RMSF errors for the SGO results were 0.83×10^{-1} , 1.30×10^{-1} , 1.31×10^{-1} , and 1.27×10^{-1} at observation angles of 0° , 15° , 30° , and 45° respectively. The results show that the solutions of the SGO at small observation angles approximate the original pulse slightly better than the solutions of the VTGPA. At the two lowest

observation angles however, the VTGPA yields a smaller RMSF. Comparing the trace errors ϵ_{trace} to the pulse field errors ϵ_{RMSF} it is difficult to establish a direct correlation between these two errors. This highlights the challenge to find a unique solution in the reconstruction problem discussed at the end of section S2.

Finally, the influence of the phase term in the complex dipole matrix element was tested. To this end, retrievals for streaking traces at an observation angle of 45° were performed, but modifying the dipole matrix element in eq. (1) of the main manuscript by adding an energy-dependent phase according to the results published in Mauritsson et al. [?]. The retrieved spectra, spectral phases, and temporal shapes (not shown) were hardly affected. In the VTGPA retrieval the RMSF without phase is 0.87×10^{-1} ; with dipole phase the RMSF is 0.89×10^{-1} . For the SGO retrievals the RMSF is 1.27×10^{-1} without dipole phase, and 1.09×10^{-1} with dipole phase. These changes in the RMSF of the reconstructed pulses are on the order of magnitude of the variations that are observed for retrievals at different observation angles. Therefore, we conclude that the inclusion or not of an energy-dependent phase into the dipole matrix element does not play a significant role for our retrievals. In view of the previous observations we conclude that the VTGPA and SGO methods are suitable for retrievals of experimental data at different observation angles. From the results of the simulated data and corresponding retrievals, we conclude that the influence of the Coulomb field, ionisation through intermediate states, and modulations of the electron yield do not hinder the pulse retrieval.

S4 Attosecond pulse retrievals from experimental traces

The retrievals were carried out for experimental streaking traces obtained from the Abel-inverted experimental images at eight different observation angles 0° , 15° , 30° , 45° , 135° , 150° , 165° , and 180° with respect to the polarisation direction. For each of the eight resulting individual streaking traces, four different post-processing methods were applied: background subtraction, background subtraction and correction of the delay-dependent total electron yield, background subtraction and fast-Fourier transform filtering (FFT filtering), and background subtraction plus yield correction plus FFT filtering. For the yield correction, the total yield was integrated in each half (left/right of the polarisation vector) of the experimental VMI images at each delay, to account for a slight drift of the total electron yield over time. The VTGPA and the SGO algorithms were applied to each of the 32 resultant experimental traces. Fig. S5 shows a set of experimental traces with background subtraction plus FFT filtering at observation angles of (a) 0° , (d) 15° , (g) 30° , and (j) 45° , and the corresponding retrieved traces with the VTGPA ((b) 0° , (e) 15° , (h) 30° , and (k) 45°), and the SGO ((c) 0° , (f) 15° , (i) 30° , and (l) 45°). Each of the figures featuring reconstructed streaking traces in Fig. S5 includes a relative error calculated according to eq. (S1).

Fig. S6 shows the reconstructed fields in the time and frequency domain corresponding to the traces in Fig. S5. Both, the VTGPA and the SGO algorithms retrieve a dominant main pulse with negative TOD. Both algorithms also retrieve satellite pulses corresponding to XUV emission from adjacent half cycles of the driving NIR pulse. The SGO algorithm retrieves slightly stronger satellites. The satellites have intensities at or below 0.1% of the main XUV pulse. The retrieved

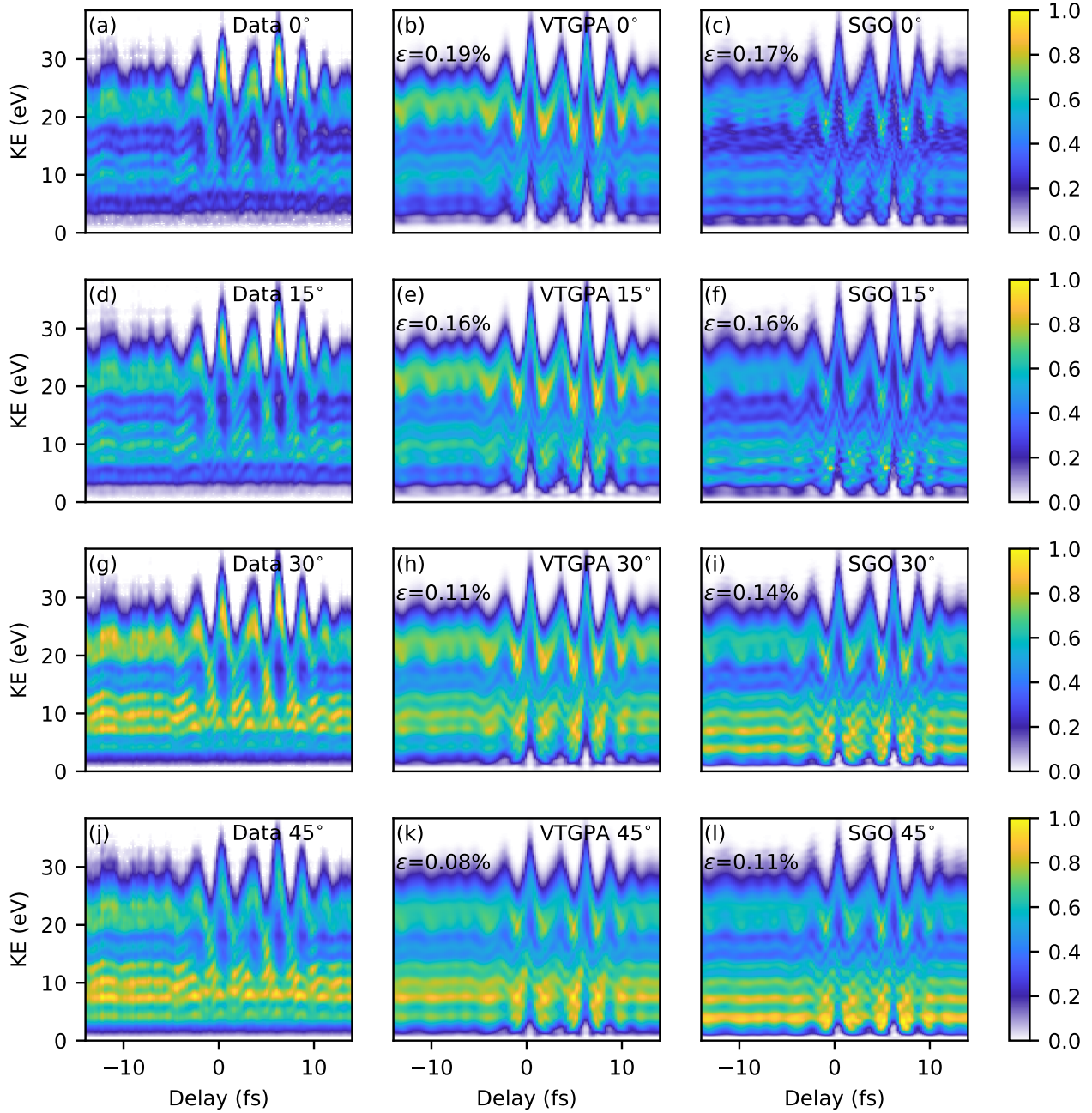


Fig. S5 | Experimental and retrieved streaking traces. left column: measured attosecond electron streaking traces at the observation angles (a) $\theta = 0^\circ$, (d) $\theta = 15^\circ$, (g) $\theta = 30^\circ$, (j) $\theta = 45^\circ$. Center column: corresponding retrieved traces with the VTGPA method: (b) $\theta = 0^\circ$, (e) $\theta = 15^\circ$, (h) $\theta = 30^\circ$, (k) $\theta = 45^\circ$. Right column: the corresponding retrieved traces with the SGO method.

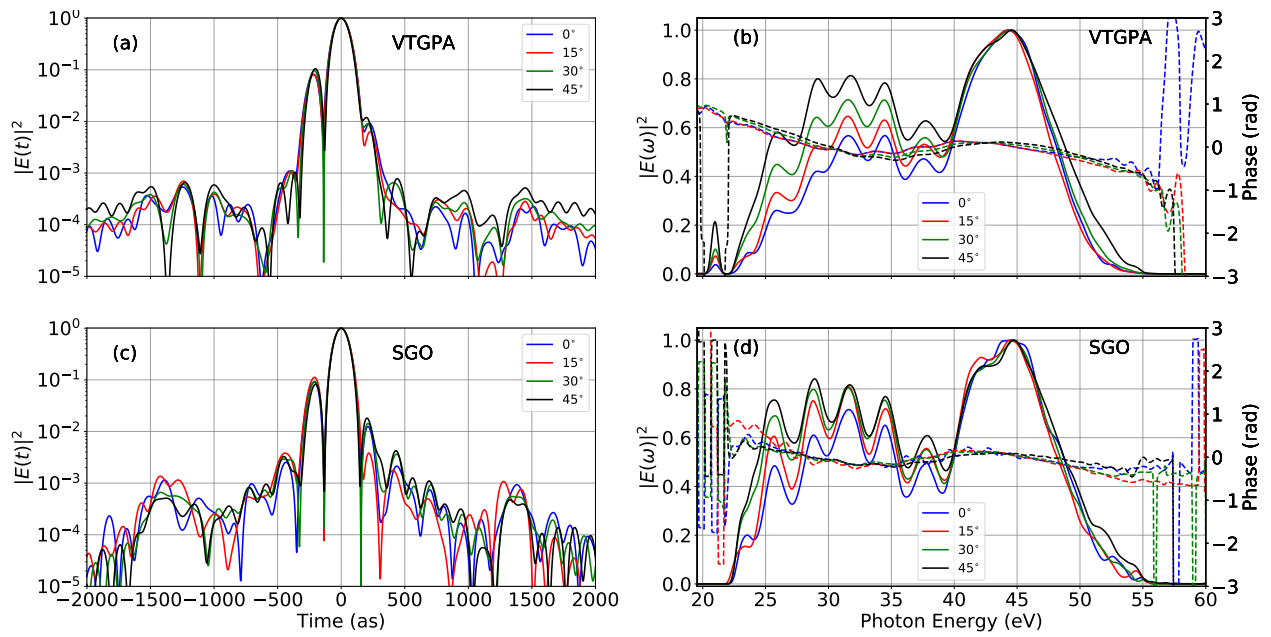


Fig. S6 | Retrieved pulses and spectra from experimental traces. Left column: temporal intensity profiles of retrieved pulses on logarithmic scale from each retrieval at different observation angles for VTGPA (a) and SGO (c). Right column: corresponding retrieved spectra (solid lines) and spectral phases (dashed lines) for VTGPA (b) and SGO (d). In all figures, the results from data at different observation angles are represented with different colors; blue: $\theta = 0^\circ$, red: $\theta = 15^\circ$, green: $\theta = 30^\circ$, black: $\theta = 45^\circ$.

spectra have a smooth component in the high energy portion, and exhibit fringes for energies below 40 eV. These fringes stem from interference between the satellites and the main pulse with the fringe spacing of ≈ 3.3 eV corresponding to half the period of the driving NIR field with a centre wavelength of $\lambda_0 = 760$ nm.

Supplementary Information References

1. Krausz, F. & Ivanov, M. Attosecond physics. *Rev. Mod. Phys.* **81**, 163 (2009). URL <http://link.aps.org/abstract/RMP/v81/p163>.
2. Hentschel, M. *et al.* Attosecond metrology. *Nature* **414**, 509–513 (2001). URL <https://www.nature.com/articles/35107000>.
3. Krausz, F. & Stockman, M. I. Attosecond metrology: from electron capture to future signal processing. *Nature Photonics* **8**, 205–213 (2014). URL <https://www.nature.com/articles/nphoton.2014.28>.
4. Lépine, F., Ivanov, M. Y. & Vrakking, M. J. J. Attosecond molecular dynamics: fact or fiction? *Nature Photonics* **8**, 195–204 (2014). URL <https://www.nature.com/articles/nphoton.2014.25>.
5. Ullrich, J. *et al.* Recoil-ion and electron momentum spectroscopy: reaction-microscopes. *Reports on Progress in Physics* **66**, 1463–1545 (2003). URL <https://doi.org/10.1088/0034-4885/66/9/203>.
6. Boguslavskiy, A. E. *et al.* The Multielectron Ionization Dynamics Underlying Attosecond Strong-Field Spectroscopies. *Science* **335**, 1336–1340 (2012). URL <https://science.sciencemag.org/content/335/6074/1336>. Publisher: American Association for the Advancement of ScienceSection: Report.

7. Cavalieri, A. L. *et al.* Attosecond spectroscopy in condensed matter. *Nature* **449**, 1029–1032 (2007). URL <http://www.nature.com/nature/journal/v449/n7165/abs/nature06229.html>.
8. Chew, S. H. *et al.* Time-of-flight-photoelectron emission microscopy on plasmonic structures using attosecond extreme ultraviolet pulses. *Applied Physics Letters* **100**, 051904 (2012). URL <http://scitation.aip.org/content/aip/journal/apl/100/5/10.1063/1.3670324>.
9. Krebs, M. *et al.* Towards isolated attosecond pulses at megahertz repetition rates. *Nature Photonics Letters* **7**, 555–559 (2013). URL <https://www.nature.com/articles/nphoton.2013.131>.
10. Itatani, J. *et al.* Attosecond streak camera. *Phys. Rev. Lett.* **88**, 173903 (2002). URL <https://link.aps.org/doi/10.1103/PhysRevLett.88.173903>.
11. Ferray, M. *et al.* Multiple-harmonic conversion of 1064 nm radiation in rare gases. *Journal of Physics B: Atomic, Molecular and Optical Physics* **21**, L31–L35 (1988). URL <https://doi.org/10.1088/0953-4075/21/3/001>.
12. Corkum, P., Burnett, N. & Ivanov, M. Subfemtosecond pulses. *Optics Letters* **19**, 1870–1872 (1994). URL <https://doi.org/10.1364/OL.19.001870>.
13. Antoine, P., L’Huillier, A. & Lewenstein, M. Attosecond pulse trains using high-order harmonics. *Phys. Rev. Lett.* **77**, 1234–1237 (1996). URL <https://link.aps.org/doi/10.1103/PhysRevLett.77.1234>.

14. Corkum, P. B. Plasma perspective on strong field multiphoton ionization. *Phys. Rev. Lett.* **71**, 1994–1997 (1993). URL <https://link.aps.org/doi/10.1103/PhysRevLett.71.1994>.
15. Sansone, G. *et al.* Isolated single-cycle attosecond pulses. *Science* **314**, 443–446 (2006). URL <http://science.sciencemag.org/content/314/5798/443>.
16. Kim, K. T. *et al.* Photonic streaking of attosecond pulse trains. *Nature Photonics* **7**, 651–656 (2013). URL <https://www.nature.com/articles/nphoton.2013.170>.
17. Pfeifer, T. *et al.* Generating coherent broadband continuum soft-X-ray radiation by attosecond ionization gating. *Optics Express* **15**, 17120–17128 (2007). URL <http://www.opticsexpress.org/abstract.cfm?URI=oe-15-25-17120>.
18. Uiberacker, M. *et al.* Attosecond real-time observation of electron tunnelling in atoms. *Nature* **446**, 627–632 (2007). URL <https://www.nature.com/articles/nature05648>.
19. Goulielmakis, E. *et al.* Real-time observation of valence electron motion. *Nature* **466**, 739–743 (2010). URL <http://www.nature.com/nature/journal/v466/n7307/abs/nature09212.html>.
20. Sansone, G. *et al.* Electron localization following attosecond molecular photoionization. *Nature* **465**, 763–766 (2010). URL <http://www.nature.com/nature/journal/v465/n7299/abs/nature09084.html>.
21. Nisoli, M. *et al.* Compression of high-energy laser pulses below 5 fs. *Opt. Lett.* **22**, 522–524 (1997). URL <http://ol.osa.org/abstract.cfm?URI=ol-22-8-522>.

22. Sabbar, M. *et al.* Combining attosecond XUV pulses with coincidence spectroscopy. *Review of Scientific Instruments* **85**, 103113 (2014). URL <http://aip.scitation.org/doi/abs/10.1063/1.4898017>.
23. Cattaneo, L. *et al.* Attosecond coupled electron and nuclear dynamics in dissociative ionization of H₂. *Nature Physics* **1** (2018). URL <https://www.nature.com/articles/s41567-018-0103-2>.
24. Vos, J. *et al.* Orientation-dependent stereo Wigner time delay and electron localization in a small molecule. *Science* **360**, 1326–1330 (2018). URL <http://science.sciencemag.org/content/360/6395/1326>.
25. Stockman, M. I., Kling, M. F., Kleineberg, U. & Krausz, F. Attosecond nanoplasmonic-field microscope. *Nature Photonics* **1**, 539–544 (2007). URL <https://www.nature.com/articles/nphoton.2007.169>.
26. Okell, W. A. *et al.* Temporal broadening of attosecond photoelectron wavepackets from solid surfaces. *Optica* **2**, 383–387 (2015). URL <http://www.opticsinfobase.org/optica/abstract.cfm?URI=optica-2-4-383>.
27. Furch, F. J. *et al.* Close to transform-limited, few-cycle 12μJ pulses at 400 kHz for applications in ultrafast spectroscopy. *Opt. Express* **24**, 19293–19310 (2016). URL <http://www.opticsexpress.org/abstract.cfm?URI=oe-24-17-19293>.
28. Rothhardt, J., Demmler, S., Hädrich, S., Limpert, J. & Tünnermann, A. Octave-spanning OPCPA system delivering CEP-stable few-cycle pulses and 22W of average power at

- 1 MHz repetition rate. *Opt. Express* **20**, 10870–10878 (2012). URL <http://www.opticsexpress.org/abstract.cfm?URI=oe-20-10-10870>.
29. Prinz, S. *et al.* CEP-stable, sub-6 fs, 300-kHz OPCPA system with more than 15 W of average power. *Opt. Express* **23**, 1388–1394 (2015). URL <http://www.opticsexpress.org/abstract.cfm?URI=oe-23-2-1388>.
30. Matyschok, J. *et al.* Temporal and spatial effects inside a compact and CEP stabilized, few-cycle OPCPA system at high repetition rates. *Opt. Express* **21**, 29656–29665 (2013). URL <http://www.opticsexpress.org/abstract.cfm?URI=oe-21-24-29656>.
31. Furch, F. J. *et al.* CEP-stable few-cycle pulses with more than 190 μ J of energy at 100 kHz from a noncollinear optical parametric amplifier. *Optics Letters* **42**, 2495–2498 (2017). URL <https://www.osapublishing.org/abstract.cfm?uri=ol-42-13-2495>.
32. Hrisafov, S. *et al.* High-power few-cycle near-infrared OPCPA for soft X-ray generation at 100 kHz. *Opt. Express* **28**, 40145–40154 (2020). URL <http://www.opticsexpress.org/abstract.cfm?URI=oe-28-26-40145>.
33. Lavenu, L. *et al.* High-power two-cycle ultrafast source based on hybrid nonlinear compression. *Optics Express* **27**, 1958–1967 (2019). URL <https://www.osapublishing.org/oe/abstract.cfm?uri=oe-27-3-1958>. Publisher: Optical Society of America.
34. Hädrich, S. *et al.* 500 W, 5 mJ, 6 fs, CEP-stable few-cycle pulses: An update on the ELI-ALPS HR2 beamline (Conference Presentation). In Dong, L. (ed.) *Fiber Lasers XVII: Technology*

- and Systems*, vol. 11260. International Society for Optics and Photonics (SPIE, 2020). URL <https://doi.org/10.1117/12.2544603>.
35. Müller, M. *et al.* Multipass cell for high-power few-cycle compression. *Optics Letters* **46**, 2678–2681 (2021). URL <https://www.osapublishing.org/ol/abstract.cfm?uri=ol-46-11-2678>. Publisher: Optical Society of America.
36. Pupeikis, J. *et al.* Water window soft X-ray source enabled by a 25 W few-cycle 2.2 μm OPCPA at 100 kHz. *Optica* **7**, 168–171 (2020). URL <http://www.osapublishing.org/optica/abstract.cfm?URI=optica-7-2-168>.
37. Thiré, N. *et al.* Highly stable, 15 W, few-cycle, 65 mrad CEP-noise mid-IR OPCPA for statistical physics. *Opt. Express* **26**, 26907–26915 (2018). URL <http://www.opticsexpress.org/abstract.cfm?URI=oe-26-21-26907>.
38. Neuhaus, M. *et al.* 10 W CEP-stable few-cycle source at 2 μm with 100 kHz repetition rate. *Opt. Express* **26**, 16074–16085 (2018). URL <http://www.opticsexpress.org/abstract.cfm?URI=oe-26-13-16074>.
39. Elu, U. *et al.* High average power and single-cycle pulses from a mid-IR optical parametric chirped pulse amplifier. *Optica* **4**, 1024–1029 (2017). URL <http://www.osapublishing.org/optica/abstract.cfm?URI=optica-4-9-1024>.
40. Mero, M. *et al.* 43 W, 1.55 μm and 12.5 W, 3.1 μm dual-beam, sub-10 cycle, 100 kHz optical parametric chirped pulse amplifier. *Opt. Lett.* **43**, 5246–5249 (2018). URL <http://ol.osa.org/abstract.cfm?URI=ol-43-21-5246>.

41. Harth, A. *et al.* Compact 200 kHz HHG source driven by a few-cycle OPCPA. *Journal of Optics* **20**, 014007 (2017).
42. Witting, T., Furch, F. J. & Vrakking, M. J. Spatio-temporal characterisation of a 100 kHz 24 W sub-3-cycle NOPCPA laser system. *Journal of Optics* **20**, 044003 (2018). URL <http://stacks.iop.org/2040-8986/20/i=4/a=044003>.
43. Hoff, D. *et al.* Continuous every-single-shot carrier-envelope phase measurement and control at 100 kHz. *Opt. Lett.* **43**, 3850–3853 (2018). URL <http://ol.osa.org/abstract.cfm?URI=ol-43-16-3850>.
44. Osolodkov, M. *et al.* Generation and characterisation of few-pulse attosecond pulse trains at 100 kHz repetition rate. *Journal of Physics B: Atomic, Molecular and Optical Physics* **53**, 194003 (2020). URL <https://iopscience.iop.org/article/10.1088/1361-6455/aba77d>. Publisher: IOP Publishing.
45. Witting, T. *et al.* Characterization of high-intensity sub-4-fs laser pulses using spatially encoded spectral shearing interferometry. *Optics Letters* **36**, 1680–2 (2011). URL <http://www.opticsinfobase.org/ol/abstract.cfm?uri=ol-36-9-1680>.
46. Ghafur, O. *et al.* A velocity map imaging detector with an integrated gas injection system. *Review of Scientific Instruments* **80**, 033110 (2009). URL <https://aip.scitation.org/doi/full/10.1063/1.3085799>.

47. Lewenstein, M., Balcou, P., Ivanov, M. Y., L'Huillier, A. & Corkum, P. B. Theory of high-harmonic generation by low-frequency laser fields. *Phys. Rev. A* **49**, 2117–2132 (1994). URL <https://link.aps.org/doi/10.1103/PhysRevA.49.2117>.
48. Mairesse, Y., & Quere, F. Frequency-resolved optical gating for complete reconstruction of attosecond bursts. *Physical Review A* **71**, 011401 (2005). URL <http://link.aps.org/doi/10.1103/PhysRevA.71.011401>.
49. Keathley, P. D., Bhardwaj, S., Moses, J., Laurent, G. & Kärtner, F. X. Volkov transform generalized projection algorithm for attosecond pulse characterization. *New J. Phys.* **18**, 073009 (2016). URL <http://stacks.iop.org/1367-2630/18/i=7/a=073009>.
50. Patchkovskii, S., Vrakking, M. J. J., Villeneuve, D. M. & Niikura, H. Selection of the magnetic quantum number in resonant ionization of neon using an XUV-IR two-color laser field. *J. Phys. B* 134002 (2020). URL <https://iopscience.iop.org/article/10.1088/1361-6455/ab82e0>.
51. Dorrer, C. & Walmsley, I. A. Accuracy criterion for ultrashort pulse characterization techniques: application to spectral phase interferometry for direct electric field reconstruction. *J. Opt. Soc. Am. B* **19**, 1019–1029 (2002). URL <https://doi.org/10.1364/JOSAB.19.001019>.
52. Varjú, K., Johnsson, P., Mauritsson, J., L'Huillier, A. & López-Martens, R. Physics of attosecond pulses produced via high harmonic generation. *American Journal of Physics* **77**, 389 (2009). URL <https://aapt.scitation.org/doi/10.1119/1.3086028>.

53. Suda, A., Hatayama, M., Nagasaka, K. & Midorikawa, K. Generation of sub-10-fs, 5-mJ-optical pulses using a hollow fiber with a pressure gradient. *Applied Physics Letters* **86**, 111116 (2005). URL <https://aip.scitation.org/doi/10.1063/1.1883706>.
54. Okell, W. A. *et al.* Carrier-envelope phase stability of hollow fibers used for high-energy few-cycle pulse generation. *Optics Letters* **38**, 3918–3921 (2013). URL <http://ol.osa.org/abstract.cfm?URI=ol-38-19-3918>.
55. Hickstein, D. D., Gibson, S. T., Yurchak, R., Das, D. D. & Ryazanov, M. A direct comparison of high-speed methods for the numerical Abel transform. *Review of Scientific Instruments* **90**, 065115 (2019). URL <https://aip.scitation.org/doi/10.1063/1.5092635>.
56. Ryazanov, M. *Development and implementation of methods for sliced velocity map imaging. Studies of overtone-induced dissociation and isomerization dynamics of hydroxymethyl radical (CH₂OH and CD₂OH)*. Ph.D. thesis, University of Southern California, Los Angeles (2012). URL <https://digitalibrary.usc.edu/asset-management/2A3BF169XWB4>.
57. Ryazanov, M. & Reisler, H. Improved sliced velocity map imaging apparatus optimized for H photofragments. *The Journal of Chemical Physics* **138**, 144201 (2013). URL <https://aip.scitation.org/doi/10.1063/1.4798929>. Publisher: American Institute of Physics.